Senescence Induced by Nox4 Expressed Aberrantly in Osteoclast Precursors Accelerates Ostoeclastogenesis to Promote Osteoarthritis

Bin Yu (yubin@smu.edu.cn)
Southern Medical University
Ke shen
Nanfang Hospital, Southern Medical University https://orcid.org/0000-0002-8656-6296
Hanjun Qin
Nanfang Hospital, Southern Medical University
Xiaonan Liu
Souhtern Medical University https://orcid.org/0000-0003-3661-7961
Lei Wang
Nanfang Hospital, Southern Medical University
Siying He
Nanfang Hospital, Southern Medical University
Xingqi Zhao
Nanfang Hospital, Southern Medical University
Jun Yang
Nanfang Hospital, Southern Medical University
Shengnan Wang
Nanfang Hospital, Southern Medical University

Article

Keywords:

Posted Date: June 23rd, 2022

DOI: https://doi.org/10.21203/rs.3.rs-1750917/v1

Abstract

Abnormal bone remodeling of subchondral bone is associated with osteoclast formation during early osteoarthritis (OA) while senescent phenotypes are detected during osteoclast differentiation. However, the associations between cellular senescence and osteoclastogenesis remain unclear in early OA. The present study found that Nox4 positively regulated the senescence of OCPs to promote multinucleated osteoclastogenesis. Overexpression of Nox4 induced overproduction of ROS, thereby promoting senescence of OCPs. Senescent OCPs secreted SASP factors to spread the senescence in OCPs clusters, over-activating the TRAF6/MAPK/c-Fos/NFATc1 axis to accelerate the fusion and osteoclast differentiation. Interestingly, the senescence of OCPs mediated by Nox4/ROS may be an essential step in initiating osteoclast differentiation. Compared to WT mice, subchondral bone loss was reduced in early OA and cartilage degeneration alleviated throughout the course of OA in Nox4-deficient mice. In addition, pharmacological inhibition of Nox4 significantly delayed OA development. In conclusion, we have identified Nox4-induced cellular senescence as an important regulator of osteoclast differentiation, suggesting that it might be a potential target to retard or prevent OA.

Introduction

Disability is a likely outcome in patients with advanced Osteoarthritis (OA), the most common chronic and degenerative disease worldwide[1,2]. Specific interventions in early OA may greatly improve the prognosis of the patients. Unfortunately, study into the early pathological mechanism of OA is still lacking[3].

Strong evidence supports that subchondral bone remodeling occurs before articular cartilage degeneration in early OA[4,5]. Bone resorption and bone formation are uncoupled in OA, dynamically shifting from early osteoclast-mediated bone resorption to late osteoblast-mediated bone formation[6,7]. Previous studies have shown that osteoclasts, as the only cells with bone resorption in vivo, are significantly active in subchondral bone in early OA[8,9]. Therefore, we believe that intervention in osteoclast formation may be a feasible way to control the progression of early OA.

Osteoclast precursors (OCPs), which are thought to be the source of osteoclasts[10], recruit TNF receptor-associated factor 6 (TRAF6) in response to macrophage colony-stimulating factor (m-CSF) and receptor activator of NF kB ligand (RANKL)[11]. TRAF6 activates mitogen-activated protein (MAP) kinase[12], activator protein-1 (AP-1)[13], and NF-kB[14] which in turn induce the expression of two key osteoclast transcription factors, c-Fos and nuclear factor-activated T cell 1 (NFATc1), initiating osteoclastic differentiation[15–17]. Recent studies have shown that osteoclasts exhibit senescent phenotypes during differentiation[18–20] and on the other hand reversing the effects on the senescence of osteoclasts may retard osteoclastogenesis[19]. However, the relationship between cellular senescence and osteoclastic differentiation has not been clarified.

Cellular senescence is a variety of dynamic and heterogeneous cellular states[21]. Senescent cells often show cell cycle arrest (upregulation of p21 cip1 and p16 INK4A and loss of Ki67)[22–24], heterochromatin changes (spatial relocalization of perinuclear H3K9me3-positive heterochromatin and SAHF formation)[25,26], increased senescence-associated β-galactosidase (SA-β-Gal) activity[27,28] and senescence-associated secretory phenotypes (SASP, such as IL-1α, IL-1β, IL-6, TNF-α, etc.)[29–31]. One essential factor that triggers the senescence is shown to be increased oxidative stress[32], and knockout of redox-sensitive transcription factor (Nrf2) in mice exhibits aging phenotypes resulting from a decline in antioxidant pathways[33,34]. However, few studies have addressed the effect of redox on bone remodeling in the subchondral bone. We have known that Nox family is a significant source of intracellular ROS[35,36]. As a unique member of Nox family, constitutively active Nox4 produces ROS[37], playing a role in the senescence of vascular cells[38]. However, it is unclear whether Nox4 is involved in the expression of senescent phenotypes during osteoclast differentiation. We, thus, hypothesized that clarification of the relationships between Nox4, cellular senescence, and remodeling of subchondral bone at early OA may be conducive to understanding the early pathological mechanism of OA.

The present study found abnormal expression of Nox4 in subchondral bone OCPs in early OA, accompanied by significant oxidative stress, cellular senescence, and osteoclast formation in OA patients and animal models. Altogether, our GEO sequencing analyses and in vivo and in vitro experiments showed that Nox4/ROS induced the senescence of OCPs, which secreted SASP factors to spread the senescence in OCPs clusters, over-activating the TRAF6/MAPK/c-Fos/NFATc1 axis to promote the fusion and differentiation of cellular clusters into multinucleated osteoclasts. Moreover, the senescence of OCPs mediated by Nox4/ROS may be an essential step in initiating osteoclast differentiation. As has been shown, Nox4 may play a crucial role in the early progression of OA, and interference with such a molecular target may be a feasible intervention.

Results

1. OCPs in subchondral bone exhibit senescent phenotypes in early OA

Given that osteoclasts (OCs) are involved in the abnormal subchondral bone resorption during early OA[39], we investigated whether cellular senescence might occur in osteoclast precursors (OCPs). Damage to articular cartilage was slightly more severe in the area of osteoarthritic mild damage (MD-OA) than in the relatively normal area (RN) (Fig. 1a). Osteoarthritis Research Society International (OARSI) score was increased slightly in the MD-OA (Fig. 1b). In situ fluorescence analysis of the subchondral bone tissue sections revealed a much greater number of $p16^+$ $RANK^+$ cells and $p21^+$ $RANK^+$ cells in the MD-OA than in the RN (Fig. 1c, d). In contrast to RN, more $RANK^+$ cells expressed p16 and p21 in MD-OA (Fig. 1c, d). To further evaluate subchondral bone changes during OA progression, we generate a destabilized anterior cruciate ligament transection (ACLT) OA mouse model. SA-β-Gal staining of the tibial tissue sections found that SA-β-Gal^+ cells increased in subchondral bone at 2 weeks after ACLT but decreased at 4 weeks

(Fig. 1e, f). Consistently, an increase in the number of $p16^+$ or $p21^+$ OCPs was detected at 2 weeks after ACLT, and subsequently a decrease at 4 weeks after ACLT (Fig. 1g, h).

The above data showed that OCPs in subchondral bone underwent senescence in early OA.

2. Oxidative stress promotes senescence of OCPs

To test whether ROS accumulation may induce senescence of OCPs, sections of subchondral bone tissue were DCFDA-stained. Results showed numbers of ROS increased at 2 weeks after ACLT and declined at 4 weeks after ACLT (Fig. 2a, b). In vitro experiments were further performed to test the possibility of direct regulation of cellular senescence by oxidative stress in OCPs. The results showed that p16 and p21 expression increased in OCPs with H2O2 concentration and decreased by NAC, regarded as a ROS inhibitor. (Fig. 2c, d). The number of EdU^+ OCPs was reduced when H2O2 was added concomitantly with M-CSF at the beginning of the culture (Fig. 2e, f). Consistently, cell proliferation marker Ki67 expression was reduced (Fig. 2g, h). NAC successfully rescued the proliferative capacity reduction effects of H2O2 (Fig. 2e-h). An increased number of SA-β-Gal^+ cells was detected in the cells with H2O2 relative to cells with control-treated and H2O2-NAC-treated (Fig. 2i, j). SAHF is a senescence-associated biomarker enriched for constitutive heterochromatin markers like H3K9me3[25]. We further detected the heterochromatin reorganization in H2O2-treated cells relative to control-treated cells as indicated by H3K9me3 staining. SAHFs in these cells were evident as large and irregularly shaped nuclear puncta, which decreased in cells treated with NAC (Fig. 2k, l). Collectively, these data demonstrate that oxidative stress may promote senescence of OCPs.

3. Nox4 expression is elevated in OCPs during early OA

mRNA expression files of 50 normal and OA samples were downloaded from the GEO database (GSE51588). After models of lateral subchondral bone were excluded, we divided the remaining samples into a non-OA group and an OA group, from each of which two male and two female knee samples were selected for analysis. Using the R package limma (version 3.40.6) for differential analysis, a screening method for differential expression based on generalized linear models, we obtained 1063 up-regulated genes and 776 down-regulated genes in the comparisons between the non-OA and the OA groups (Fig. 3a). The heatmap showed the expression levels of all the differentially expressed genes in each sample (Fig. 3b). The results showed a significantly different distribution of transcriptional profiles between the non-OA and the OA groups. On the other hand, clustering analysis of the samples justified our grouping of non-OA and OA samples. Furthermore, we searched for genes enriched for the terms senescence and oxidative stress and found that Nox4 was widely involved in oxidative stress, reactive oxygen species production, and cell senescence (Fig. 3c). To validate our results of GEO analysis, we performed immunohistochemical and immunofluorescence staining of the bone tissue sections using a specific antibody against Nox4. Nox4-expressing cells were more abundant in the subchondral bone from the MD-OA than from the RN (Fig. 3d top, e top). Interestingly, we found the Nox4 expression in OCPs was elevated in the subchondral bone from the MD-OA compared to the RN (Fig. 3d bottom, e bottom).

Consistently, the Nox4 expression was substantially elevated in OCPs in the subchondral bone in mice 2 weeks after ACLT in comparison with the sham group but inhibited by GKT137831 (Fig. 3f, g). Therefore, the data clearly demonstrate that Nox4 may be mainly expressed in OCPs in the subchondral bone of OA patients.

4. Nox4 regulates ROS concentration to promote OCPs senescence and osteoclast differentiation

To identify whether nox4 might induce the OCPs senescence by producing ROS, we generated lentivirus overexpressing Nox4 (LV-Nox4) and lentiviral vectors exclusively containing the GFP gene (LV-GFP) (Fig. 4a). The expression levels of Nox4 in OCPs treated as described above were detected by western blot analysis, which showed that Nox4 protein was overexpressed in Nox4-transfected-OCPs (Fig. 4b). DHE staining to label ROS found higher ROS concentrations in Nox4-overexpressed OCPs than in GFP-transfected OCPs (Fig. 4c, d). This finding confirms that Nox4 may promote ROS generation in OCPs.

Then we tried to confirm the senescence of OCPs in response to ROS produced by Nox4 overexpression. The SA-β-Gal staining showed more SA-β-Gal$^+$ cells in Nox4-transfected OCPs relative to GFP-transfected OCPs, but the number of SA-β-Gal$^+$ cells decreased with the presence of NAC (Fig. 4e, f). In Nox4-transfected OCPs, we detected more SAHF formation, fewer Ki67$^+$ cells and EdU$^+$ cells than GFP-transfected OCPs (Fig. 4g-l top, middle). NAC rescued all the above phenomena (Fig. 4g-l bottom). Western blot analysis showed that RANKL-treated OCPs elevated p16 and p21 expression, and Nox4 overexpression further increased their expression levels (Fig. 4m). NAC reduced p16 and p21 expression induced by either RANKL-treated or Nox4-overexpression (Fig. 4m).

After we determined the promotive effect of ROS produced by Nox4 on OCPs senescence, we further examined whether the ROS produced by Nox4 may accelerate osteoclast differentiation in early OA. The previous DHE staining confirmed that RANKL stimulated the OCPs group to produce more ROS, which was already excessively produced in the Nox4-transfected OCPs group (fig. 4c). Interestingly, we found that the osteoclast differentiation markers like TRAF6, c-Fos, CtsK, and NFATc1 showed a trend consistent with senescence markers (Fig. 4m). These data suggest that senescence induced by excessive ROS in OCPs may be an essential procedure in the initiation of osteoclast differentiation. We found that overexpression of Nox4 accelerated the fusion of multinucleated TRAP$^+$ osteoclasts (Fig. 4n top, o left top), and increased actin belts (Fig. 4n middle, o right top) and lacunae on the bone slices (Fig. 4n bottom, o bottom), confirming the differentiation of osteoclasts mediated by RANKL. Conversely, the treatment with NAC decreased the ROS generated by overexpression of Nox4 to suppress osteoclast differentiation (Fig. 4n right).

All these data suggest that Nox4 may generate ROS to promote OCPs senescence and osteoclast differentiation.

5. Senescent OCPs induced by Nox4 secrete SASP to promote osteoclast differentiation

Senescent cells have a complex senescence-associated secretory phenotype (SASP), involving a range of pro-inflammatory factors with significant paracrine effects on cell and tissue biology[29]. We examined whether SASP might be a bridge between senescence and osteoclast differentiation. Our qPCR showed such SASP factors as IL-1α, IL-1β, IL-6, MMP3 and TNF-α were elevated in Nox4-overexpressing OCPs (Fig. 5a). To clarify the roles of the factors, we induced osteoclast differentiation in OCPs untreated which were cultured in the supernatant medium of OCPs transfected with GFP or Nox4 and stimulated with M-CSF and RANKL. The number of $TRAP^+$ multinucleated osteoclasts and F-actin belts increased, and more clefts were detected on the seeded bone pieces in the OCPs treated with Nox4-overexpressing supernatant (Fig. 5b-e).

As for the pathways for osteoclast differentiation, it has been reported that the interaction of RANKL with RANK recruits TRAF6 to activate a signal cascade of various mitogen activated protein kinases (MAPKs), upregulating NFATc1[40]. An activator protein (AP)-1 complex containing c-Fos is required for the autoamplification of NFATc1, enabling the robust induction of NFATc1[41]. To verify the activation of the above cascade, we used the supernatant containing SASP from Nox4-overexpressing OCPs to stimulate OCPs untreated. The western blot showed that TRAF6, c-Fos, and NFATc1 were excessively activated in the OCPs treated with SASP, M-CSF, and RANKL (Fig. 5f). Moreover, CtsK, a resorption protease, was elevated in the OCPs with stimulation of SASP (Fig. 5f). Therefore, we further assessed whether the MAPK pathway might be involved in osteoclast differentiation stimulated by SASP. We found that SASP elevated the phosphorylation levels of MAPK family markers like p38, ERK1/2, and JNK at the beginning of osteoclast differentiation (Fig. 5g). Consistent with our previous finding that NAC inhibited Nox4-induced senescence of OCPs and decreased SASP secretion (Fig. 4m, 5a), MAPK phosphorylation was attenuated in the OCPs cultured in the supernatant of OCPs overexpressing Nox4 treated by NAC (Fig. 5h). At 2 weeks post-ACLT, the expression levels of P-ERK, P-p38, and P-JNK were enhanced in $RANK^+$ OCPs in the tibial subchondral bone and reduced by GKT137831 by nearly 2-fold, 2-fold, and 3-fold, respectively (Fig. 5i, j). Therefore, our in vivo and in vitro work demonstrate that Nox4/ROS may promote secretion of the SASP which stimulates excessive osteoclast differentiation at early OA through the TRAF6/MAPK/c-Fos/NFATc1 axis.

6. Osteoclast differentiation is dependent on Nox4-induced senescence

The above findings lead us to further exploration of whether the process of osteoclast differentiation may be dependent on Nox4-induced cell senescence. DHE staining showed that ROS concentration was decreased in Nox4-knockout OCPs with or without RANKL stimulation (Fig. 6a, b). Western blot analysis showed that senescence markers like p16 and p21, and osteoclast differentiation markers like NFATc1, TRAF6, CtsK, and c-Fos were reduced in Nox4-knockout OCPs after RANKL stimulation compared with WT OCPs (Fig. 6c, d). In addition, the phosphorylation level of the MAPK pathway in Nox4-knockout OCPs was decreased in contrast to WT OCPs (Fig. 6e). Moreover, after RANKL stimulation, the number of $TRAP^+$ multinucleated osteoclasts and actin belts was reduced, and the overall bone resorption capacity also attenuated in Nox4-knockout OCPs (Fig. 6f, g). Consistently, exogenous addition of H2O2 restored

the osteoclast differentiation capacity of Nox4-knockout OCPs (Fig. 6h). The above data have confirmed that knockout of Nox4 may reduce ROS concentration, inhibiting the senescence of OCPs to retard osteoclastogenesis.

7. Knockout of Nox4 inhibits OCPs senescence and osteoclastogenesis to retarred bone remodeling

To further characterize the specific role of Nox4 activation in the subchondral bone OCPs in OA development, we generated mice with ablation of Nox4. Co-immunofluorescence-staining showed $p21^+$ $rank^+$ cells and $p16^+$ $rank^+$ cells were decreased in $Nox4^{-/-}$ mice relative to WT mice at 2 weeks post-ACLT and these positive cells were much fewer at 4 weeks than at 2 weeks after surgery (Fig. 7a, b). Consistently, SA-β-Gal staining showed the same changes (Fig. 7c, d). As expected, a significant reduction in the number of osteoclasts was observed in both strains of mice at 4 weeks after surgery compared with 2 weeks. In contrast to WT mice with Nox4 activation in OCPs, fewer $TRAP^+$ osteoclasts were observed in the subchondral bone of $Nox4^{-/-}$ mice at 2 or 4 weeks after surgery (Fig. 3e, f). Moreover, μ-CT analysis showed much less abnormality in the subchondral bone of $Nox4^{-/-}$ mice than in the WT mice which exhibited a reduction in bone mass at 2 weeks after surgery but an aberrant rise at 4 weeks (Fig. 3g-h). The low-bone-mass phenotype in the tibial subchondral bone at 2 weeks after surgery was characterized by a decrease in BV/TV, BS/BV, BMD, and Tb. Th, and an increase in Tb. Pf, but all these were reversed at 4 weeks (Fig. 3h). We then explored whether maintaining subchondral bone homeostasis by deletion of Nox4 in OCPs may rescue ACLT-induced damage in articular cartilage. Safranin O and H&E staining showed that ACLT led to a gradual degeneration of articular cartilage from 2 to 4 weeks after surgery in WT littermates, but this effect was blunted in the $Nox4^{-/-}$ mice (Fig. 3i-j). Taken together, these results further support the hypothesis that Nox4 activation in OCPs plays a critical role in aberrant subchondral bone loss, suggesting that targeted inhibition of Nox4 in subchondral OCPs may prevent cartilage degeneration and post-traumatic OA development.

8. Administration of GKT137831 in vivo ameliorates OA progression

Now that the role of Nox4 in early OA progression had been determined, we explored whether clinical drugs targeting Nox4 might delay the progression of OA in 3 groups of mice: one subjected to sham operation, one to ACLT and one to ACLT+gavage with GKT137831 for 2 weeks after ACLT. More $TRAP^+$ OCs were observed in the tibial subchondral bone in the mice undergoing ACLT than in those undergoing sham operation, but this early OA phenotype was decreased by GKT137831 treatment (Fig. 8a, b). μ-CT analysis also showed that the low-bone-mass phenotypes in the tibial subchondral bone, characterized by low trabecular BV/TV (Fig. 8d), BS/BV (Fig. 8e), BMD (Fig. 8f) and Tb. Th (Fig. 8g), and high Tb. Sp as well (Fig. 8h), were all rescued by GKT137831 treatment 2 weeks after surgery (Fig. 8c–h). Notably, in response to ACLT, the tibial subchondral bone of mice showed phenotypes of mild proteoglycan loss (Fig. 8i), increased OARSI score (Fig. 8j), and decreased calcified cartilage (CC) and hyaline cartilage (HC) ratio (Fig. 8k, l). GKT137831, however, was verified to ameliorate these phenotypes (Fig. 8i-l). All the data here clearly demonstrated that GKT137831 might have rescued osteoclastogenesis and bone resorption during early OA.

Discussion

Our hypothesis assumed a relationship between nox4, senescence and osteoclast differentiation in the pathological mechanism of early OA. As illustrated in Fig. 9, our experiments confirmed, for the first time, that Nox4 mediated senescence of OCPs to facilitate osteoclast differentiation, leading to the loss of subchondral bone in early OA.

Nox4, a molecule closely related to cellular senescence and oxidative stress[38,42,43], is detected in previous reports to induce autophagy which directly promotes osteoclast differentiation[44]. However, differentiation of osteoclasts, unlike that of other kinds of cells, involves the aggregation and fusion of entire cellular clusters[45]. Consistently, we found that not all OCPs highly expressed Nox4 in the subchondral bone at a certain time point in early OA, suggesting that the process when Nox4 promotes the fusion and differentiation of OCPs clusters may involve intercellular signaling.

The prior research into the intercellular signaling find that a pathway for the osteoclast–chondrocyte crosstalk, described as pro-inflammatory factors released from subchondral bone like IL-1β[46], TNF-α[47,48], IL-6[49] and CXCL12[50,51], regulates osteoclast differentiation. In addition, senescent chondrocytes produce pro-inflammatory SASP and catabolic enzymes potentially modulating the behavior of subchondral osteoclast lineage cells[52,53]. On the other hand, there is increasing evidence to support the conclusion that remodeling of subchondral bone precedes cartilage degeneration[9,54,55], which implies cytokines secreted by senescent chondrocytes may not be the chief trigger for the differentiation of osteoclasts in early OA. Our present study not only found more evidence to support the above conclusion but also proposed a new initial mechanism for osteoclast differentiation driven by senescence. We found that senescence of OCPs was dependent on Nox4 in the subchondral bone in early OA and that senescent OCPs induced OCPs cluster fusion and differentiation into multinucleated osteoclasts through paracrine secretion of SASP factors.

Specifically, we found that the expression of p16 and p21 increased with the time of osteoclast differentiation induced by RANKL, implying that the senescence might have been extended in the OCPs clusters upon the stimulation of SASP. During RANKL stimulation, the expression of senescence markers was decreased in $Nox4^{-/-}$ OCPs compared with WT OCPs, suggesting that Nox4-induced senescence may be a critical link in the osteoclast differentiation. Consistently, recent sequencing results confirm that preosteoclasts undergo a significant arrest in the cell cycle and alteration in the metabolic status during differentiation.[56] In addition, our results also confirmed that OCPs increased the expression of p16 and p21 after RANKL-induced differentiation. Considering all these senescence phenotypes found in the process of osteoclastogenesis, we speculate that the senescence in OCPs may be a precursor state in osteoclast differentiation. Therefore, the relationship between nox4, senescence and osteoclast differentiation can be described in the present study as follows: Nox4 may induce the aberrant senescent OCPs that secrete SASP in turn to accelerate the premature senescence of the whole OCPs clusters which pushes osteoclast differentiation.

Interestingly, recent studies have shown that the KDM4B-CCAR1-MED1 signaling axis induces the formation of tartrate-resistant acid phosphatase-positive multinucleate cells through H3K9 demethylation[57]. However, our results observed increased H3K9me3-labeled SAHF in OCPs during differentiation. In fact, the two phenomena are not contradictory. Growing evidence supports the independence between inhibitory histone marks and chromatin compaction during the formation of the aging heterochromatin layer[26], suggesting that formation of higher-order heterochromatin and epigenetic remodeling of the genome may be discrete events. As a heterochromatin marker[58], H3K9me3 is demethylated near the promoters of osteoclast-related[57] and SASP-related genes on the chromosomes of senescent OCPs[59], promoting the expression of related genes. However, H3K9me3 maintains a conservative methylation status at the locations of genes associated with cell proliferation[60]. At the same time, the condensation of dispersing H3K9me3 during the compaction of higher-order heterochromatin promotes the formation of SAHF evident in cellular fluorescence[26].

After we characterized the critical role of Nox4 in the senescence and differentiation of OCP, we constructed an ACLT model in Nox4 knockout mice. Consistently, the senescence and osteoclast differentiation of OCPs were significantly restrained and bone resorption activity was reduced in early OA subchondral bone in $Nox4^{-/-}$ mice. In addition, we observed reduced articular cartilage degeneration in $Nox4^{-/-}$ mice compared with WT mice due to the maintenance of subchondral bone homeostasis. These in vivo results support our finding above that Nox4-mediated OCP senescence promotes osteoclast differentiation, thereby accelerating the process of subchondral bone turnover in early OA.

Besides knockout of Nox4, we also used GKT137831, a dual inhibitor of Nox1/4, to treat the mice that underwent ACLT. GKT137831 has been used to treat fibrotic nephropathy, idiopathic pulmonary fibrosis, and primary biliary cholangitis[61]. We found that GKT137831 significantly inhibited the abnormal activity of osteoclasts in subchondral bone at early OA, thus hindering the development of OA.

Unfortunately, it is a limitation of the present study that we used the sequencing data from the GEO database to screen out the molecule Nox4 in this study. Because the data were typically from the patients with advanced OA who had undergone arthroplasty, the functional differences the data showed in cellular senescence were less pronounced than those the early OA patients might have shown compared to normal people, although oxidative stress was functionally enriched in the advanced OA patients. In addition, we selected Nox4 systemic knockout mice because our time-gradient subchondral bone fluorescence co-staining showed that Nox4 expression was mainly elevated in OCPs in early OA. However, the systemic knockout mice might have made our observation not as absolutely precise as the specific knockout mice.

In conclusion, our present study discovers a novel pathomechanism by which Nox4 acts on subchondral bone OCPs to mediate OA pathogenesis. Nox4 expression is elevated in a subset of OCPs in early OA and induces OCPs senescence through the production of excess ROS. On one hand, the senescence of OCPs mediated by Nox4/ROS may be an essential step in initiating osteoclast differentiation. On the other

hand, senescent OCPs secrete SASP factors to spread the senescence in OCPs clusters, over-activating the TRAF6/MAPK/c-Fos/NFATc1 axis in OCPs to accelerate the fusion of whole cellular clusters and osteoclast differentiation. Furthermore, knockdown of Nox4 significantly reduces OCPs senescence and osteoclastogenesis, thereby interfering with subchondral bone turnover in early OA. Finally, because GKT137831, a potent Nox4 inhibitor, improves subchondral bone microarchitecture and reduces OA progression, it may be a potential target in the therapy for patients with OA.

Materials And Methods

Human samples

Six human samples of the tibial plateaus were obtained from the OA patients who had undergone knee replacement surgery with approval from the Ethics Committee of Nanfang Hospital, Southern Medical University. The lateral portion of the tibial plateau that did not show significant wear was used as a control. Three levels of the sample sections were processed for each patient in histological examination and OARSI scoring as described previously. The number of positively stained cells in the subchondral bone was counted in 3 different areas for each patient in each group.

Mice

Wild-type (WT; $Nox4^{+/+}$) and Nox4-deficient (C57BL/6N-$Nox4^{em1cyagen}$; $Nox4^{-/-}$) mice of C57BL/6 background were purchased from Cyagen Biosciences (Guangzhou, China). The transgenes were genotyped using the following primer pairs: 5’-ATTGGAGGGACAAGTTCTGATAG-3’, 5’-GAGGAGTCTTGTGGAAGAGTATG-3’, and 5’-CAAGTTCATGTTTCTCTTCTCTCTG-3’.

C57BL/6J (wild-type) mice were purchased from the Experimental Animal Center of Southern Medical University (Guangzhou, China). Unless otherwise stated, all mice were 12 weeks old and maintained on a sterile diet and autoclaved water in specific pathogen-free housing facilities at Southern Medical University (Guangzhou, China). Male mice were used for all in vitro experiments. All experiments were approved by the Southern Medical University Animal Care and Use Committee.

Mice knee OA model induced by anterior cruciate ligament transection (ACLT)

ACLT was performed on 12-week-old mice to induce abnormal mechanical loading-related OA in the knee joint, according to a previous study[62]. A sham operation was only opening the joint capsule and then suturing the incision. Mice were housed under standard conditions with 12-hour light and 12-hour dark cycles and fed and watered ad libitum in a temperature-controlled room. To examine the effect of GKT137831 on early OA, we made comparisons between the sham operation mice, ACLT mice and mice undergoing gavage with GKT137831 (60 mg/kg/d) after ACLT for two weeks.

Tissue sampling and preparation

All mice were euthanized by 1.2% tribromoethanol before sampling at 2 and 4 weeks post-ACLT (n=8). The mice knee joints freshly dissected were fixed in 4% paraformaldehyde at 4°C for 24 hours and then decalcified in 0.5 M EDTA (pH 7.4) for 7 days. Tissue was embedded in paraffin (3.5 μm) and OCT (18 μm) and sectioned continuously.

Micro-CT analysis

Knee specimens were exanimated by a high-resolution μ-CT scanner (SkyScan 1172, Bruker) with a voltage of 55 kV, a current of 145 mA, and a resolution of 12 μm per pixel. The longitudinal images of the medial tibial plateau were used for 3D reconstruction and histomorphometry analysis, with the entire medial compartment of the subchondral bone as region of interest. The 3D structural parameters included: relative bone volume or bone volume fraction (BV/TV), ratio of bone surface area to bone volume (BS/BV), bone mineral density (BMD), trabecular thickness (Tb.Th), and trabecular bone pattern factor (Tb.Pf).

Histochemistry, immunohistochemistry, and histomorphometric analysis

Serial sections were dewaxed in xylene, hydrated with graded ethanol, and stained with Safranin O/Fast Green and H&E as previously reported[62]. TRAP staining (Wako 294-67001, Japan) was performed according to the manufacturer's instructions, followed by restaining with methyl green. Next, immunohistochemical staining was performed following standard protocols. After dewaxing and hydration, 0.01 M sodium citrate buffer (ph 6.0) was used for antigen retrieval, and 3% hydrogen peroxide to reduce endogenous peroxidase activity. Tissue sections were permeabilized with 0.1% Triton X-100 before they were blocked in 10% goat serum to reduce nonspecific staining and then incubated with anti-Nox4 (Abcam, ab133303, 1/500) at 4°C overnight. A horseradish peroxidase-streptavidin detection system (Dako) was used to restain the sections with hematoxylin (Dako). Micrographs of sections were captured by the ortho-fluorescence microscope (Olympus DP71). We quantified articular cartilage degeneration in the tibial plateau joint using the OARSI scoring system as described previously[55]. The distance from the tideline to the subchondral bone plate (SBP) was measured as the thickness of calcified cartilage, and the distance from the tideline to the articular cartilage surface as the thickness of hyaline cartilage. Quantitative histomorphometric analysis was performed blinded using the software Image J (ImageJ 1.53). The number of positively stained cells was counted in the entire subchondral bone region of the tibia in each specimen and in five sequential sections per mouse in each group.

SA-β-Gal staining and immunofluorescence staining of bone tissue sections

Senescent cells were detected using the Senescence β-Gal Staining Kit (Cell Signaling Technology, #9860) according to the manufacturer's instructions and photographed with an ortho-fluorescent microscope (Olympus, DP71). For immunofluorescence staining, after dewaxing hydration, antigen retrieval, permeabilizing, and non-specific site closure, the paraffin sections were stained with anti-RANK (Abcam, ab13918, 1:200), anti-p16 (Proteintech, 10883-1-AP, 1:200), anti-p21 (Cell Signaling Technology, #2947, 1:200), anti-Nox4 (Abcam, ab133303, 1:200), anti-P-p38 (Cell Signaling Technology, #4511,

1:1000), anti-P-ERK1/2 (Cell Signaling Technology, #4370, 1:1000), and anti-P-JNK (Cell Signaling Technology, #4668, 1:1000) at 4 °C overnight. Then the sections were incubated with fluorescent secondary antibodies (Abbkine, A23210 & A23420, 1:200) at 37 °C for 1 hour. Cell nuclei were re-stained with DAPI (Solarbio, S2110) and observed under a confocal microscope (Zeiss, LSM 980). Analyzed were the data of 8 mice for each treatment group and 5 different regions of the tibial subchondral bone for each sample.

Cell culture, viral infections and osteoclast differentiation

As previously described[21], bone marrow cells (BMMs) were isolated from the femur and tibia of 4-week-old male mice, screened and induced into osteoclast precursors (OCPs). Briefly, whole bone marrow cells were isolated by flushing the bone marrow cavities of the femur and tibia before cultured in α-MEM (Gibco) containing 10% serum (Gibco), and 1% penicillin-streptomycin (HyClone) for 24 hours. Floating cells collected were cultured with 70 ng/mL M-CSF (PeproTech, 315-02-10) for 48 hours to induce OCPs formation. OCPs were transfected using a lentivirus overexpressing Nox4 (GeneCopoeia, LPP-Mm06833-Lv201-400) or negative control (GeneCopoeia, LPP-NEG-Lv201-400). Successful gene overexpression was confirmed by immunoblot analysis. To induce the formation of mature osteoclasts, OCPs were cultured with 70 ng/mL M-CSF and 100 ng/mL RANKL (PeproTech, 315-11C-10) for 6 days. We used the TRAP staining kit (Sigma, 387A-1KT) to stain the mature osteoclasts differentiated from OCPs according to the manufacturer's instructions. $TRAP^+$ osteoclasts with 5 or more nuclei were counted. To obtain the supernatants containing SASP factors, we collected the medium of transfected-OCPs treated with or without 2 mM NAC for 24 hours. H_2O_2, NAC and RANKL were added into SASP-containing medium to culture untreated OCPs for durations indicated in the figure legends.

RANKL and NAC treatment started the third day after complete transfection in transfected OCPs while RANKL was stimulated 2 days after formation of knockout OCPs. The above cell incubations were performed in a humidified incubator at 37 °C and 5% CO2, if not additionally indicated.

Cell proliferation assay

BMMs seeded in 96-well plates at 30% confluency were incubated with M-CSF at 37 °C for 2 days to induce OCPs formation. After respective treatments, cell proliferation was determined using an EdU imaging kit (UElandy, C6016) according to the manufacturer's instructions. The absorbance at 555 nm were observed under an inverted fluorescence microscope (Olympus, IX73). EdU assays were performed in triplicate each time and repeated three times.

Measurement of ROS

Tissue ROS levels were measured using the OxiSelect in vitro ROS/RNS detection kit (Cell Biolabs, STA-347). Frozen tissue sections were thawed at room temperature for 15 minutes, incubated with 20 μmol/L dichlorofluorescein diacetate at 37 °C for 20 minutes, washed and mounted, and observed under an upright fluorescence microscope (Olympus, BX63) (excitation wavelength, 485 nm; emission wavelength,

535 nm). Starved OCPs were incubated with dihydroethidium (KeyGEN, KGAF019, 1:1000) at 37 °C for 15 minutes, washed, and stimulated with M-CSF and α-MEM with or without RANKL for 15 minutes. Fluorescence images (excitation wavelength, 518 nm; emission wavelength, 605 nm) were acquired in an inverted fluorescence microscope (Olympus, IX73).

Determination of bone resorption

After suspension BMMs seeded on bone slices (IDS, DT-1BON1000-96) were induced into OCPs after 2 days of M-CSF stimulation, the OCPs were induced to differentiate into osteoclasts with 70 ng/ml M-CSF and 100 ng/ml RANKL for 10 days. Bone slices were washed with 6% sodium hypochlorite and PBS. The absorption pit area on the air-dried disk was observed under a microscope and measured with ImageJ (ImageJ 1.53).

Cellular immunofluorescence

The cells were inocubated on the cell slides for culture. Fresh cells were fixed with 4% paraformaldehyde and permeabilized with 0.1% Triton X-100. After washing, non-specific binding sites were blocked with 10% goat serum for 1 hour and overnight at 4 °C in the dark with anti-H3K9me3 (Cell Signaling Technology, # 13969) or anti-Ki67 (Abcam, ab15580). Fluorescent secondary antibodies (Abbkine, A23210 & A23420) functioned together for 1 hour at 37 ° C. Then, the cell slides were removed and sealed with DAPI. Phalloidin (AAT Bioquest, AAT-23119) was additionally added to mark the F-actin belts during the secondary antibody incubation phase. A confocal microscope (Zeiss, LSM 980) was used for the above observation and software Image J (ImageJ 1.53) for calculation.

Real-time quantitative PCR and microarray analysis

To determine the expression levels of SASP factors in GFP-transfected OCPs, Nox4-transfected OCPs and Nox4-transfected OCPs with NAC, total RNA was extracted using the EZ-press RNA purification kit (EZBioscience, B0004D) according to the manufacturer's instructions, for reverse transcription using Color Reverse Transcription Kit (EZBscience, A0010CGQ), and qPCR using 2 × Color SYBR Green qPCR Master Mix (EZBscience, A0012-R2) in ABI QuantS tudio5 (Applied Biosystems, QuantStudio5). The relative expression of each target gene was calculated using the 2-ΔΔCt method. Details of the primers are listed below.

IL-1α: F-5'-CGAAGACTACAGTTCTGCCATT-3', and R-5'-GACGTTTCAGAGGTTCTCAGAG-3'; IL-1β: F-5'-GCAACTGTTCCTGAACTCAACT-3', and R-5'-ATCTTTTGGGGTCCGTCAACT-3'; IL-6: F-5'-TAGTCCTTCCTACCCCAATTTCC-3', and R-5'-TTGGTCCTTAGCCACTCCTTC-3'; MMP3: F-5'-ACATGGAGACTTTGTCCCTTTTG', and R-5'-TTGGCTGAGTGGTAGAGTCCC-3'; TNF-α: F-5'-CCCTCACACTCAGATCATCTTCT-3', and R-5'- GCTACGACGTGGGCTACAG-3'.

Western blot analysis

Total protein was extracted using a total protein extraction kit (KeyGEN, KGP2100) and diluted with loading buffer (Pythonbio, AAPR39). Proteins (15 μg) were separated using SDS-Page and electrotransferred to a polyvinylidene difluoride (PVDF) membrane. After blocking, each membrane was incubated with a primary antibody at 4 ° C overnight and then with a secondary antibody corresponding to the host species of the primary antibody for 1 hour at room temperature. A luminescent substrate (Millipore, WBKLS0500) was used for visualization. Antibodies used were as follows: anti-p21 (Cell Signaling Technology, # 2947, 1:1000), anti-p16 (Proteintech, 10883-1-AP, 1:600), anti-Nox4 (Huabio, ET1607-4, 1:600), anti-NFATc1 (Santacruz, sc-7294, 1:200), anti-TRAF6 (Santacruz, sc-8409, 1:200), anti-c-Fos (Cell Signaling Technology, #2250, 1:1000), anti-CatK (Santacruz, sc-48353, 1:200), anti-β-actin (Abmart, m20011, 1:2000), anti-P-p38 (Cell Signaling Technology, #4511, 1:1000), anti-p38 (Cell Signaling Technology, #8690, 1:1000), anti-p-JNK (Cell Signaling Technology, #4668, 1:1000), anti-JNK (Proteintech, 66210-1-Ig, 1:600), anti-p-ERK1/2 (Cell Signaling Technology, #4370, 1:1000), anti-ERK1/2 (Cell Signaling Technology, #4695, 1:1000).

Microarray Data

The microarray expression profiling dataset GSE51588, based on the GPL13497 platform, was downloaded from the Gene Expression Omnibus (GEO, https://www.ncbi.nlm.nih.gov/geo/). The sequencing included 50 samples the data of which had been normalized, 10 from human non-OA knees and 40 from human OA knees. To better characterize OA, we screened the samples according to the following criteria: (1) the medial tibial plateau; (2) male: female = 1:1; (3) normal: OA patients = 1:1; (4) eligible patients randomized. Consequently, 4 samples from human non-OA knees and 4 ones from human OA knees were obtained as follows: GSM1248763, GSM1248764, GSM1248765, GSM1248766, GSM1248791, GSM1248798, GSM1248800, and GSM1248804.

Differentially expressed genes (DEG)

After the data of the above 8 samples log2 transformed, DEGs in the medial subchondral bone of the tibial plateau in OA knees compared to non-OA knees were selected using the limma package. $P < 0.05$ and $| log2FC | > 1$ were used as thresholds to screen differential genes.

Functional enrichment analysis of DEGs

We used Sangerbox Tools (http://vip.sangerbox.com/) for functional enrichment analysis of DEGs. We displayed the functional enrichment genes from oxidative stress and cellular senescence, and screened out the most relevant differential genes.

Statistical analysis

All images resulted from at least three independent experiments with similar results. All data were expressed as mean ± SD using GraphPad Prism 9.0.0 (GraphPad Software, San Diego, CA, USA). One-way ANOVA followed by Tukey’s t tests, two-way ANOVA followed by Tukey’s t tests or two-tailed paired

Student's t tests were used to compare the means among groups. Significance levels were set at $P < 0.05$ and indicated by "*", $P < 0.01$ by "**", and $P < 0.001$ by "***".

Declarations

Funding:

National Natural Science Foundation of China No.82001478

National Natural Science Foundation of China No.82002352

Natural Science Foundation of Guangdong Province No.2018A030313806

Natural Science Foundation of Guangdong Province No.2020A1515010145

President Foundation of Nanfang Hospital No.2020B028

Author contributions:

Ke Shen and Hanjun Qin contributed equally to this work.

Conceptualization: Ke Shen, Hanjun Qin, Xiaonan Liu

Methodology: Ke Shen, Xiaonan Liu, Xingqi Zhao

Investigation: Ke Shen, Siying He

Visualization: Ke Shen

Supervision: Bin Yu, Shengnan Wang, Lei Wang, Jun Yang

Writing—original draft: Ke Shen

Competing interests:

All other authors declare they have no competing interests.

Data and materials availability:

All data are available in the main text or the supplementary materials

References

1. Hunter, D. J., March, L. & Chew, M. Osteoarthritis in 2020 and beyond: a Lancet Commission. The Lancet **396**, 1711–1712 (2020).

2. Vos, T. *et al.* Years lived with disability (YLDs) for 1160 sequelae of 289 diseases and injuries 1990–2010: a systematic analysis for the Global Burden of Disease Study 2010. Lancet **380**, 2163–2196 (2012).
3. Hermann, W., Lambova, S. & Muller-Ladner, U. Current Treatment Options for Osteoarthritis. Curr Rheumatol Rev **14**, 108–116 (2018).
4. Lacourt, M. *et al.* Relationship between cartilage and subchondral bone lesions in repetitive impact trauma-induced equine osteoarthritis. Osteoarthritis Cartilage **20**, 572–583 (2012).
5. Boyde, A. & Firth, E. C. High resolution microscopic survey of third metacarpal articular calcified cartilage and subchondral bone in the juvenile horse: possible implications in chondro-osseous disease. Microsc Res Tech **71**, 477–488 (2008).
6. Hu, W. *et al.* Tumour dormancy in inflammatory microenvironment: A promising therapeutic strategy for cancer-related bone metastasis. Cell Mol Life Sci **77**, 5149–5169 (2020).
7. Goldring, S. R. Alterations in periarticular bone and cross talk between subchondral bone and articular cartilage in osteoarthritis. Ther Adv Musculoskelet Dis **4**, 249–258 (2012).
8. Zhen, G. & Cao, X. Targeting TGFβ signaling in subchondral bone and articular cartilage homeostasis. Trends Pharmacol Sci **35**, 227–236 (2014).
9. Zhen, G. *et al.* Inhibition of TGF-β signaling in mesenchymal stem cells of subchondral bone attenuates osteoarthritis. Nat Med **19**, 704–712 (2013).
10. Udagawa, N. *et al.* Origin of osteoclasts: mature monocytes and macrophages are capable of differentiating into osteoclasts under a suitable microenvironment prepared by bone marrow-derived stromal cells. Proc Natl Acad Sci U S A **87**, 7260–7264 (1990).
11. Bai, S. *et al.* FHL2 inhibits the activated osteoclast in a TRAF6-dependent manner. J Clin Invest **115**, 2742–2751 (2005).
12. Lee, K. *et al.* Selective Regulation of MAPK Signaling Mediates RANKL-dependent Osteoclast Differentiation. Int J Biol Sci **12**, 235–245 (2016).
13. Feng, Y. *et al.* The LIM protein, Limd1, regulates AP-1 activation through an interaction with Traf6 to influence osteoclast development. J Biol Chem **282**, 39–48 (2007).
14. Kim, B., Lee, K. Y. & Park, B. Icariin abrogates osteoclast formation through the regulation of the RANKL-mediated TRAF6/NF-κB/ERK signaling pathway in Raw264.7 cells. Phytomedicine **51**, 181–190 (2018).
15. Matsuo, K. *et al.* Fosl1 is a transcriptional target of c-Fos during osteoclast differentiation. Nat Genet **24**, 184–187 (2000).
16. Rho, T. W. *et al.* Glycyrrhizae Radix Inhibits Osteoclast Differentiation by Inhibiting c-Fos-Dependent NFATc1 Expression. Am J Chin Med **45**, 283–298 (2017).
17. Zhang, K. *et al.* A flavonoids compound inhibits osteoclast differentiation by attenuating RANKL induced NFATc-1/c-Fos induction. Int Immunopharmacol **61**, 150–155 (2018).

18. Wang, Y. *et al.* Radiation induces primary osteocyte senescence phenotype and affects osteoclastogenesis in vitro. Int J Mol Med **47**, 76 (2021).
19. Gorissen, B. *et al.* Hypoxia negatively affects senescence in osteoclasts and delays osteoclastogenesis. J Cell Physiol **234**, 414–426 (2018).
20. Lee, S. Y. *et al.* Hypoxia-inducible factor-2α mediates senescence-associated intrinsic mechanisms of age-related bone loss. Exp Mol Med **53**, 591–604 (2021).
21. Liu, X. *et al.* Osteoclasts protect bone blood vessels against senescence through the angiogenin/plexin-B2 axis. Nat Commun **12**, 1832 (2021).
22. Scholzen, T. & Gerdes, J. The Ki-67 protein: from the known and the unknown. J Cell Physiol **182**, 311–322 (2000).
23. Gerdes, J. *et al.* Cell cycle analysis of a cell proliferation-associated human nuclear antigen defined by the monoclonal antibody Ki-67. J Immunol **133**, 1710–1715 (1984).
24. Zhang, H. Molecular signaling and genetic pathways of senescence: Its role in tumorigenesis and aging. J Cell Physiol **210**, 567–574 (2007).
25. Zhang, X. *et al.* The loss of heterochromatin is associated with multiscale three-dimensional genome reorganization and aberrant transcription during cellular senescence. Genome Res **31**, 1121–1135 (2021).
26. Chandra, T. *et al.* Independence of Repressive Histone Marks and Chromatin Compaction during Senescent Heterochromatic Layer Formation. Mol Cell **47**, 203–214 (2012).
27. Dimri, G. P. *et al.* A biomarker that identifies senescent human cells in culture and in aging skin in vivo. Proc Natl Acad Sci U S A **92**, 9363–9367 (1995).
28. Debacq-Chainiaux, F., Erusalimsky, J. D., Campisi, J. & Toussaint, O. Protocols to detect senescence-associated beta-galactosidase (SA-betagal) activity, a biomarker of senescent cells in culture and in vivo. Nat Protoc **4**, 1798–1806 (2009).
29. Acosta, J. C. *et al.* A complex secretory program orchestrated by the inflammasome controls paracrine senescence. Nat Cell Biol **15**, 978–990 (2013).
30. Ritschka, B. *et al.* The senescence-associated secretory phenotype induces cellular plasticity and tissue regeneration. Genes Dev **31**, 172–183 (2017).
31. Rodier, F. *et al.* Persistent DNA damage signalling triggers senescence-associated inflammatory cytokine secretion. Nat Cell Biol **11**, 973–979 (2009).
32. Ngoi, N. YL. *et al.* The redox-senescence axis and its therapeutic targeting. Redox Biol **45**, 102032 (2021).
33. Cheung, K. L. *et al.* Nrf2 knockout enhances intestinal tumorigenesis in Apc(min/+) mice due to attenuation of anti-oxidative stress pathway while potentiates inflammation. Mol Carcinog **53**, 77–84 (2014).
34. Hayes, J. D. & Dinkova-Kostova, A. T. The Nrf2 regulatory network provides an interface between redox and intermediary metabolism. Trends Biochem Sci **39**, 199–218 (2014).

35. Park, M. W. *et al.* NOX4 promotes ferroptosis of astrocytes by oxidative stress-induced lipid peroxidation via the impairment of mitochondrial metabolism in Alzheimer's diseases. Redox Biol **41**, 101947 (2021).
36. Zhang, J. *et al.* Tumoral NOX4 recruits M2 tumor-associated macrophages via ROS/PI3K signaling-dependent various cytokine production to promote NSCLC growth. Redox Biol **22**, 101116 (2019).
37. Goettsch, C. *et al.* NADPH oxidase 4 limits bone mass by promoting osteoclastogenesis. J Clin Invest **123**, 4731–4738 (2013).
38. Salazar, G. NADPH Oxidases and Mitochondria in Vascular Senescence. Int J Mol Sci **19**, E1327 (2018).
39. Hu, W., Chen, Y., Dou, C. & Dong, S. Microenvironment in subchondral bone: predominant regulator for the treatment of osteoarthritis. Ann Rheum Dis **80**, 413–422 (2021).
40. Takayanagi, H. Osteoimmunology: shared mechanisms and crosstalk between the immune and bone systems. Nat Rev Immunol **7**, 292–304 (2007).
41. Asagiri, M. & Takayanagi, H. The molecular understanding of osteoclast differentiation. Bone **40**, 251–264 (2007).
42. Hecker, L. *et al.* Reversal of persistent fibrosis in aging by targeting Nox4-Nrf2 redox imbalance. Sci Transl Med **6**, 231ra47 (2014).
43. Piera-Velazquez, S. & Jimenez, S. A. Role of cellular senescence and NOX4-mediated oxidative stress in systemic sclerosis pathogenesis. Curr Rheumatol Rep **17**, 473 (2015).
44. Sun, J. *et al.* Nox4 Promotes RANKL-Induced Autophagy and Osteoclastogenesis via Activating ROS/PERK/eIF-2α/ATF4 Pathway. Front Pharmacol **12**, 751845 (2021).
45. Søe, K. Osteoclast Fusion: Physiological Regulation of Multinucleation through Heterogeneity-Potential Implications for Drug Sensitivity. Int J Mol Sci **21**, E7717 (2020).
46. Cao, Y. *et al.* IL-1β differently stimulates proliferation and multinucleation of distinct mouse bone marrow osteoclast precursor subsets. J Leukoc Biol **100**, 513–523 (2016).
47. Lam, J. *et al.* TNF-α induces osteoclastogenesis by direct stimulation of macrophages exposed to permissive levels of RANK ligand. J Clin Invest **106**, 1481–1488 (2000).
48. Kobayashi, K. *et al.* Tumor Necrosis Factor α Stimulates Osteoclast Differentiation by a Mechanism Independent of the Odf/Rankl–Rank Interaction. J Exp Med **191**, 275–286 (2000).
49. Kudo, O. *et al.* Interleukin-6 and interleukin-11 support human osteoclast formation by a RANKL-independent mechanism. Bone **32**, 1–7 (2003).
50. Gronthos, S. & Zannettino, A. C. W. The role of the chemokine CXCL12 in osteoclastogenesis. Trends Endocrinol Metab **18**, 108–113 (2007).
51. Su, Y.-W. *et al.* Roles of apoptotic chondrocyte-derived CXCL12 in the enhanced chondroclast recruitment following methotrexate and/or dexamethasone treatment. J Cell Physiol **236**, 5966–5979 (2021).

52. Rim, Y. A., Nam, Y. & Ju, J. H. The Role of Chondrocyte Hypertrophy and Senescence in Osteoarthritis Initiation and Progression. Int J Mol Sci **21**, 2358 (2020).
53. Engsig, M. T. *et al.* Matrix Metalloproteinase 9 and Vascular Endothelial Growth Factor Are Essential for Osteoclast Recruitment into Developing Long Bones. J Cell Biol **151**, 879–890 (2000).
54. Lin, C. *et al.* Activation of mTORC1 in subchondral bone preosteoblasts promotes osteoarthritis by stimulating bone sclerosis and secretion of CXCL12. Bone Res **7**, 5 (2019).
55. Su, W. *et al.* Angiogenesis stimulated by elevated PDGF-BB in subchondral bone contributes to osteoarthritis development. JCI Insight **5**, e135446.
56. Tsukasaki, M. *et al.* Stepwise cell fate decision pathways during osteoclastogenesis at single-cell resolution. Nat Metab **2**, 1382–1390 (2020).
57. Yi, S.-J. *et al.* The KDM4B–CCAR1–MED1 axis is a critical regulator of osteoclast differentiation and bone homeostasis. Bone Res **9**, 27 (2021).
58. Campos, E. I. & Reinberg, D. Histones: annotating chromatin. Annu Rev Genet **43**, 559–599 (2009).
59. Takahashi, A. *et al.* DNA damage signaling triggers degradation of histone methyltransferases through APC/C(Cdh1) in senescent cells. Mol Cell **45**, 123–131 (2012).
60. Yu, Y. *et al.* Targeting the Senescence-Overriding Cooperative Activity of Structurally Unrelated H3K9 Demethylases in Melanoma. Cancer Cell **33**, 322–336.e8 (2018).
61. Teixeira, G. *et al.* Therapeutic potential of NADPH oxidase 1/4 inhibitors. Br J Pharmacol **174**, 1647–1669 (2017).
62. Qin, H.-J. *et al.* SDF-1/CXCR4 axis coordinates crosstalk between subchondral bone and articular cartilage in osteoarthritis pathogenesis. Bone **125**, 140–150 (2019).

Figures

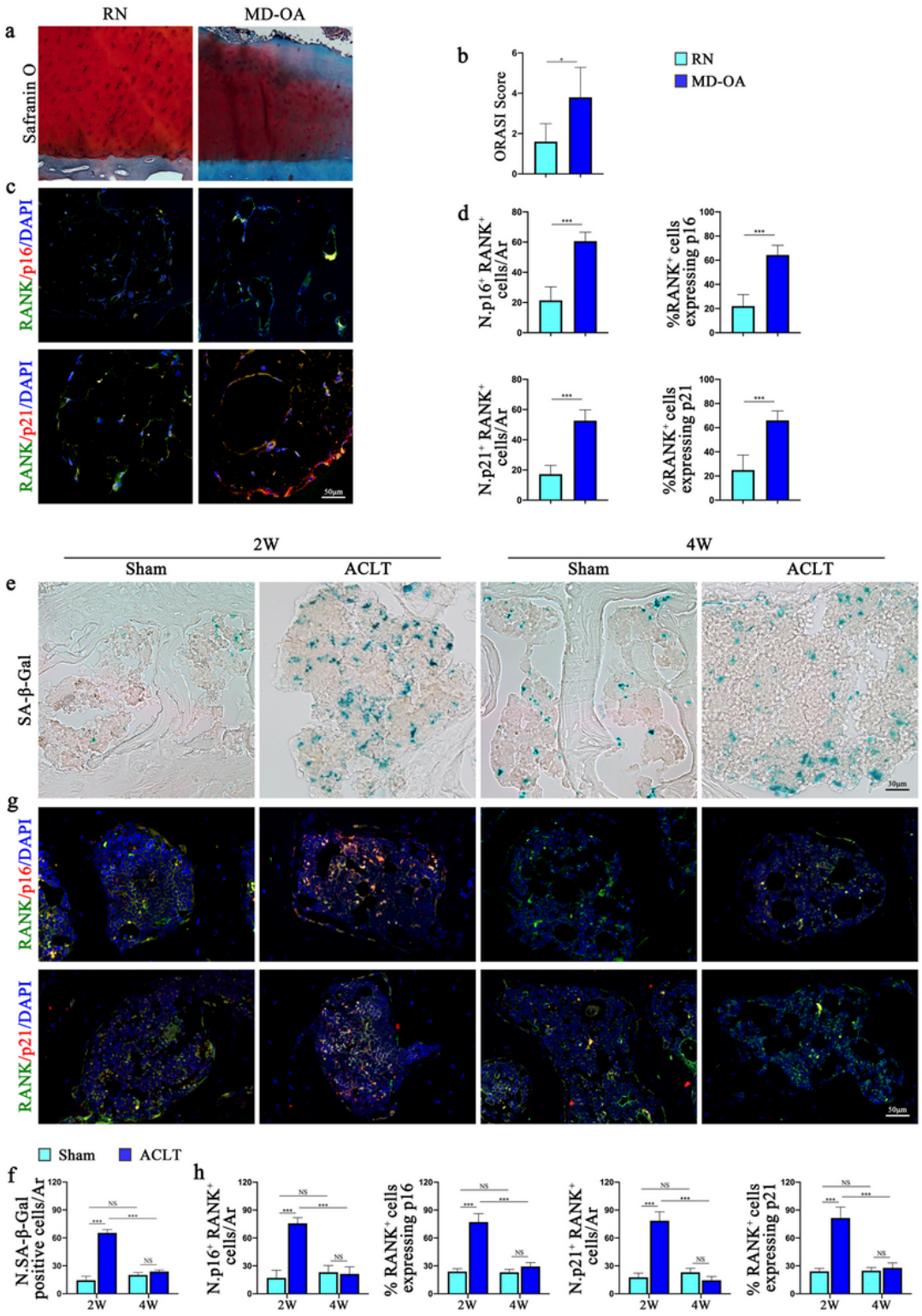

Figure 1

OCPs in subchondral bone exhibit senescent phenotypes in early OA. a-d Tibial plateau sections from OA patients undergoing joint replacement surgery. RN = relatively normal area; MD-OA = area of osteoarthritic mild damage. **a** Representative images of the RN and MD-OA sections of the human tibial plateau stained with Safranin O-Fast Green. Scale bar: 50 μm. **b** Calculation of Osteoarthritis Research Society International (OARSI) scores. **c** Immunostaining images of p16 (top) and p21 (bottom) in $RANK^+$ cells in

the RN and MD-OA in the human tibial subchondral bone. Scale bars, 50 μm. **d** Numbers of p16 and RANK double-positive cells (top left), p21 and RANK double-positive cells (bottom left) per mm^2 tissue area in the human tibial subchondral bone. Percentages of $RANK^+$ cells expressing p16 (top right) and p21 (bottom right). **e–h** Samples were harvested at 2 or 4 weeks after surgery from the three-month-old mice treated with ACLT or Sham operation. **e, f** SA-β-Gal staining of (e) and numbers of SA-β-Gal^+ cells in (h) mouse tibial subchondral bone at 2 and 4 weeks post-ACLT respectively compared with the sham control. **g** Representative images of double-immunofluorescence staining of mouse tibial subchondral bone at 2 and 4 weeks post-ACLT respectively compared with the sham control using antibodies against p16 (red, top), p21 (red, bottom), and RANK (green). Scale bar: 50 μm. **h** Numbers of p16 and RANK double-positive cells (left), p21 and RANK double-positive cells (middle right) per mm^2 tissue area in mouse tibial subchondral bone at 2 and 4 weeks post-ACLT respectively compared with the sham control. Percentages of $RANK^+$ cells expressing p16 (middle left) and p21 (right). Data are shown as mean ± s.d. and analyzed by Student's t test or two-way ANOVA. n=5, ***P < 0.001, *P < 0.05, and ns ≥ 0.05.

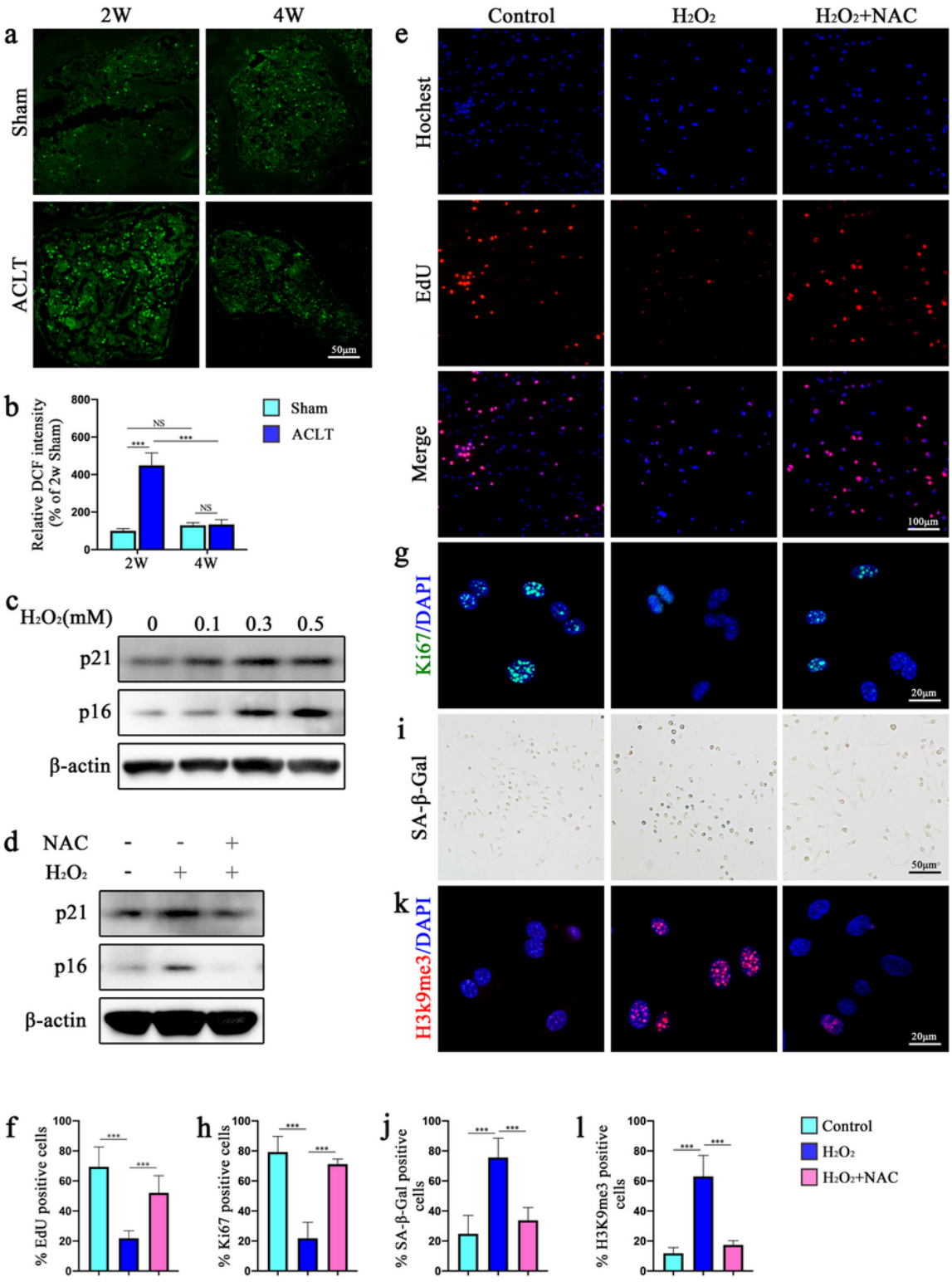

Figure 2

Oxidative stress promotes the senescence of OCPs. a-b Representative images for DCF fluorescence and relative DCF intensity in mouse tibial subchondral bone at 2 and 4 weeks post-ACLT compared with the sham control. Scale bars, 50 μm. **c-l** Bone marrow mononuclear cells and macrophages were isolated from 4-week-old C57BL/6J mice and cultured with M-CSF for 2 days to induce the formation of OCPs and treated as follows. **c** Representative immunoblot images for senescence marker proteins in OCPs

stimulated by 70ng/ml M-CSF treated with H_2O_2 at 0mM, 0.1mM, 0.3mM and 0.5mM for 24 hours. **d** Representative immunoblot images for senescence marker proteins stimulated by 70ng/ml M-CSF with or without 0.5mM H_2O_2 and 2mM NAC in OCPs for 24 hours. **e** Representative images for EdU (red) fluorescence in OCPs stimulated by 70ng/ml M-CSF with or without 0.5mM H_2O_2 and 2mM NAC in OCPs for 24 hours. Scale bars, 100 μm. **f** Percentage of EdU^+ cells in OCPs. **g, h** Representative cytofluorescence images and quantitative analysis of Ki67 (green) in OCPs in vitro. Scale bars, 20 μm. **i, j** Representative images of SA-β-Gal staining and quantitative analysis of SA-β-Gal^+ cells in OCPs in vitro. Scale bars, 50 μm. **k, l** Immunofluorescence staining of H3K9me3 (red) and percentage quantification of $H3K9me3^+$ cells. Scale bars, 20 μm. Data are shown as mean ± s.d. and analyzed by one-way ANOVA or two-way ANOVA. n=5, ***P < 0.001, and ns ≥ 0.05.

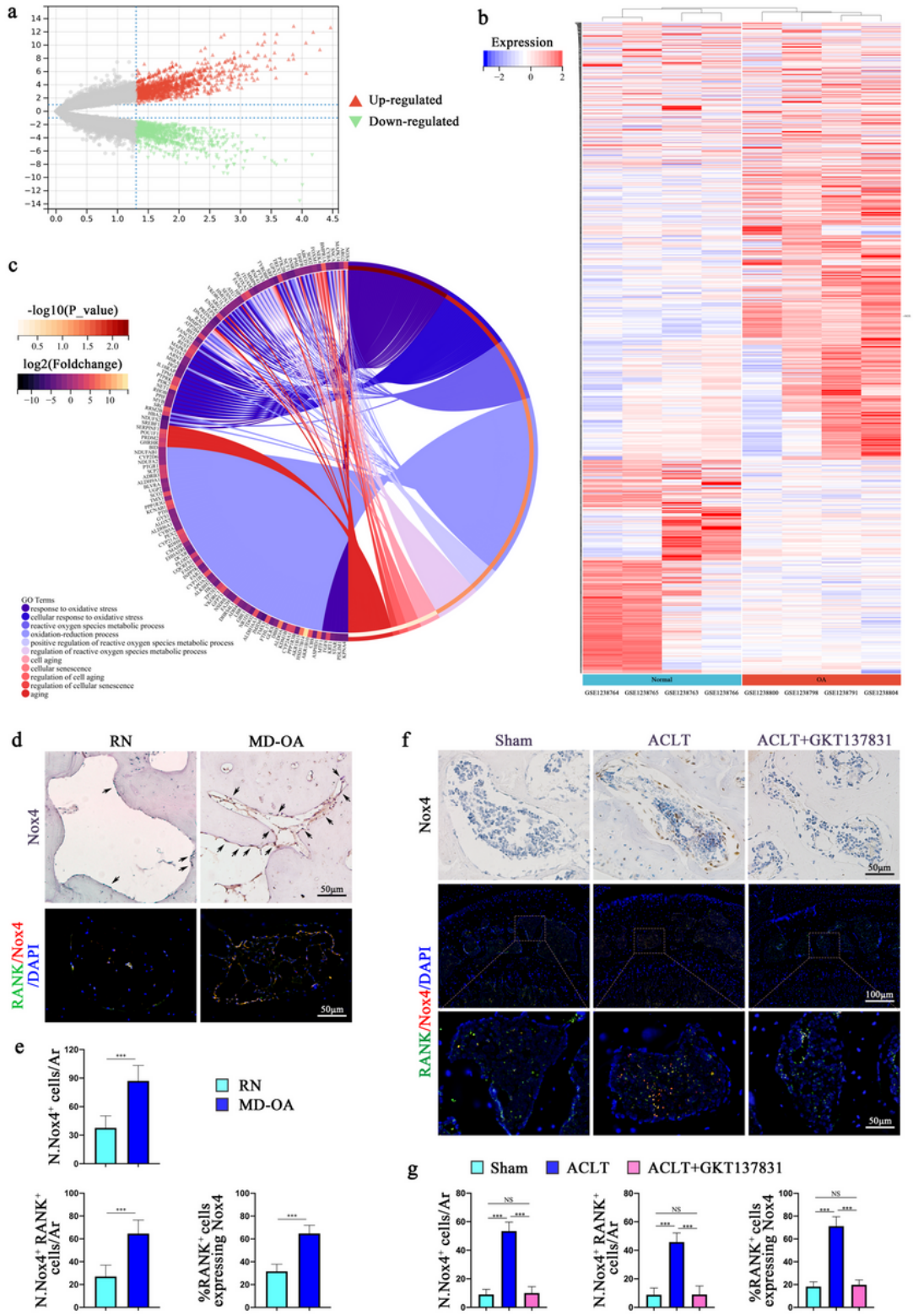

Figure 3

Nox4 expression is elevated in OCPs during early OA. a Volcano plots showed the numbers of differentially expressed genes identified from the medial subchondral bone of normal and OA patients. **b** Heatmap of differentially expressed genes in GEO dataset coloring the samples-groups. **c** GO term analysis of differentially expressed genes for senescence and oxidative stress in the medial subchondral bone of OA patients. The left hemisphere is the differential genes and expression fold while the right is

the molecular function and p value. **d, e** Representative immunostaining (**d** top) and quantitative analysis (**e** top) of $Nox4^+$ cells in tibial subchondral bone of OA patients. Double-immunofluorescence staining (**d** bottom) and quantitative analysis (**e** bottom) of tibial subchondral bone sections using antibodies against $Nox4^+$ (red) and $RANK^+$ (green). Scale bars, 50 μm. **f, g** Representative immunostaining (**f** top) and quantitative analysis (**g** left) of $Nox4^+$ cells in tibial subchondral bone of mice with sham operation, ACLT or ACLT+GKT137831 treatment. Scale bars, 50 μm. Double-immunofluorescence staining (**f** middle) and quantitative analysis (**g** middle and right) of tibial subchondral bone sections using antibodies against $Nox4^+$ (red) and $RANK^+$ (green). Scale bars, 100 μm. Boxed areas are shown at higher magnification in f bottom. Scale bars, 50 μm. Data are shown as mean ± s.d. and analyzed by Student's t test or one-way ANOVA. n=5, ***P < 0.001, and ns ≥ 0.05.

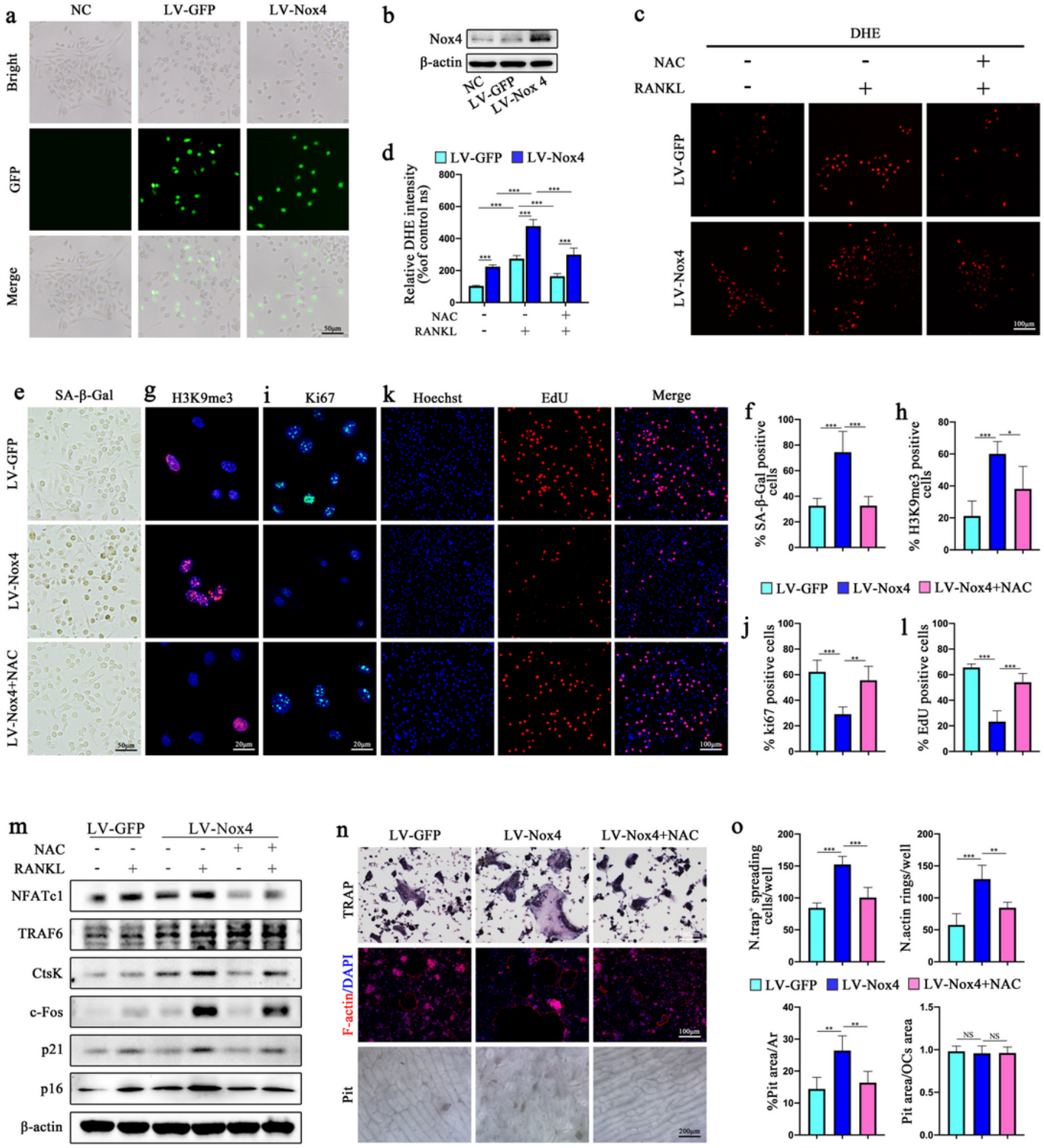

Figure 4

Nox4 regulates ROS concentration to promote OCPs senescence and osteoclast differentiation. a-o OCPs extracted from four-week-old C57BL/6N mice and transfected with lentivirus overexpressing Nox4 (LV-Nox4) and lentiviral vectors containing GFP gene (LV-GFP). The differentiation of OCPs was stimulated by 70ng/ml M-CSF and 100ng/ml RANKL. 2mM NAC was added after two-day transfection. **a** Representative images of OCPs treated with negative controls, GFP-transfected (LV-GFP) and Nox4-

transfected (LV-Nox4). Scale bar: 50 μm. **b** Representative immunoblot images of Nox4 in mouse OCPs treated with negative controls, GFP-transfected (LV-GFP) and Nox4-transfected (LV-Nox4). **c** Representative images of DHE fluorescence in Nox4-transfected or GFP-transfected OCPs stimulated with or without 100 ng/ml RANKL and 2mM NAC for 20 min. Scale bar: 100 μm. **d** Relative DHE intensity in OCPs under the indicated conditions. **e, f** Representative images of SA-β-Gal staining and quantitative analysis of SA-β-Gal$^+$ cells in OCPs stimulated by 70ng/ml M-CSF with or without 2mM NAC for 24 hours. Scale bars, 50 μm. **g, h** Immunofluorescence staining of H3K9me3 (red) and percentage quantification of H3K9me3$^+$ cells. Scale bars, 20 μm. **i, j** Immunofluorescence staining of Ki67 (green) and percentage quantification of Ki67$^+$ cells. Scale bars, 20 μm. **k, l** Representative images of EdU (red) fluorescence in OCPs stimulated by 70ng/ml M-CSF with or without 2mM NAC for 24 hours. Scale bars, 100 μm. **m** Representative immunoblot images of the marker proteins for senescence and osteoclast differentiation stimulated by 70ng/ml M-CSF with or without 100ng/ml RANKL or 2mM NAC in OCPs for 48 hours. **n** Representative images of TRAP$^+$ OCs (top, scale bar, 100 μm), actin belt formation (middle, scale bar, 100 μm) and bone resorption by OCs (bottom, scale bar, 200 μm). **o** Quantified analyses of TRAP$^+$ spreading multinucleated cells/well (top left), actin rings/well (top right), Pit area (bottom left) and Pit area/OCs area (bottom right). Data are shown as mean ± s.d. and analyzed by one-way ANOVA or two-way ANOVA. n=5, ***P < 0.001, **P < 0.01, *P < 0.05, and ns ≥ 0.05.

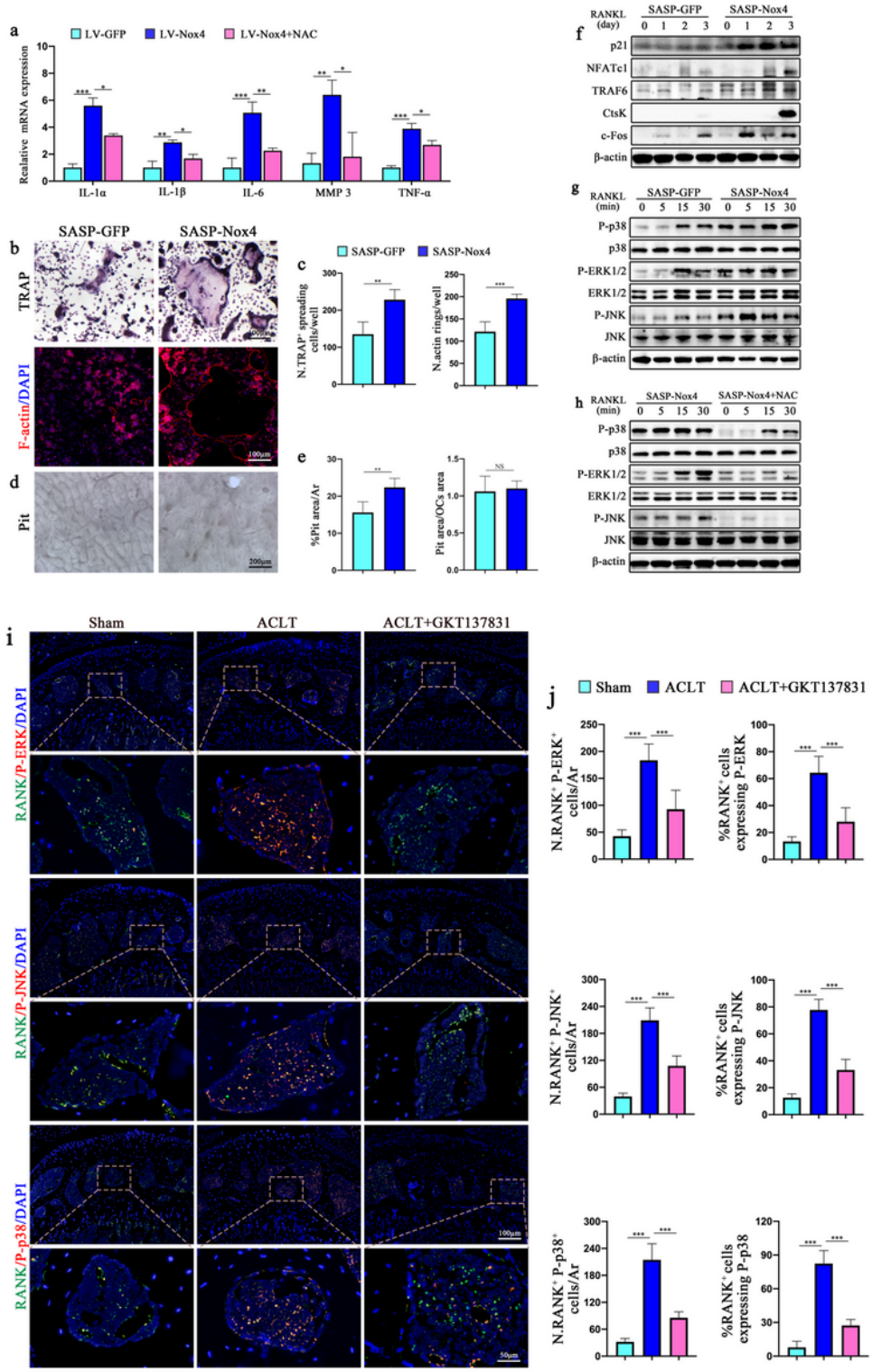

Figure 5

Senescent OCPs induced by Nox4 secrete SASP to promote osteoclast differentiation. a qPCR analysis of IL-1α, IL-1β, IL-6, MMP3, and TNF-α mRNA in Nox4-transfected OCPs stimulated by 70ng/ml M-CSF treated with or without 2mM NAC for 24 hours. **b-h** OCPs extracted from four-week-old C57BL/6N mice. The non-transfected OCPs were cultured with the medium from OCPs transfected with lentiviral vectors containing GFP gene (LV-GFP) and lentivirus overexpressing Nox4 (LV-Nox4) with or without NAC to

induce osteoclast differentiation with 70ng/ml M-CSF and 100ng/ml RANKL. **b, d** Representative images for $TRAP^+$ osteoclasts (**b** top, scale bar, 100 μm), actin belts (**b** bottom, scale bar, 100 μm), and bone resorption by osteoclasts (**d**, scale bar, 200 μm). **c, e** Quantified analyses of $TRAP^+$ spreading multinucleated cells/well (**c** left), actin rings/well (c right), Pit area (**e** left) and Pit area/OCs area (**e** right). **f** Representative immunoblot images for osteoclast differentiation marker proteins stimulated by 70ng/ml M-CSF and 100ng/ml RANKL with medium from OCPs transfected with lentivirus overexpressing Nox4 or lentiviral vectors containing GFP gene for 0, 1, 2, 3 days. **g** Representative OCPs immunoblot images for MAPK pathway marker proteins stimulated by 70ng/ml M-CSF and 100ng/ml RANKL with medium from OCPs transfected with lentivirus overexpressing Nox4 or lentiviral vectors containing GFP gene for 0, 5, 15, 30 minutes. **h** Representative OCPs immunoblot images for MAPK pathway marker proteins stimulated by 70ng/ml M-CSF, 100ng/ml RANKL and medium from OCPs transfected with lentivirus overexpressing Nox4 treated with or without 2mM NAC for 0, 5, 15, 30 minutes. **i-j** Samples harvested at 2 weeks after surgery from the three-month-old mice treated with sham operation or ACLT with or without 60mg/kg/d GKT137831. **i** Representative immunostaining of OCPs expressing MAPK pathway marker proteins in the tibial subchondral bone of OA mice with or without GKT137831. Scale bars, 100 μm. Boxed areas are shown at a higher magnification in the corresponding bottom. Scale bars, 50 μm. **j** Numbers of MAPK pathway marker proteins and RANK double positive cells (left) and percentages of $RANK^+$ cells expressing MAPK pathway marker proteins (right) per mm^2 tissue area in the mice tibial subchondral bone at 2 weeks post-ACLT with or without GKT137831. Data are shown as mean ± s.d. and analyzed by Student's t test or one-way ANOVA. n=5, ***P < 0.001, **P < 0.01, *P < 0.05, and ns ≥ 0.05.

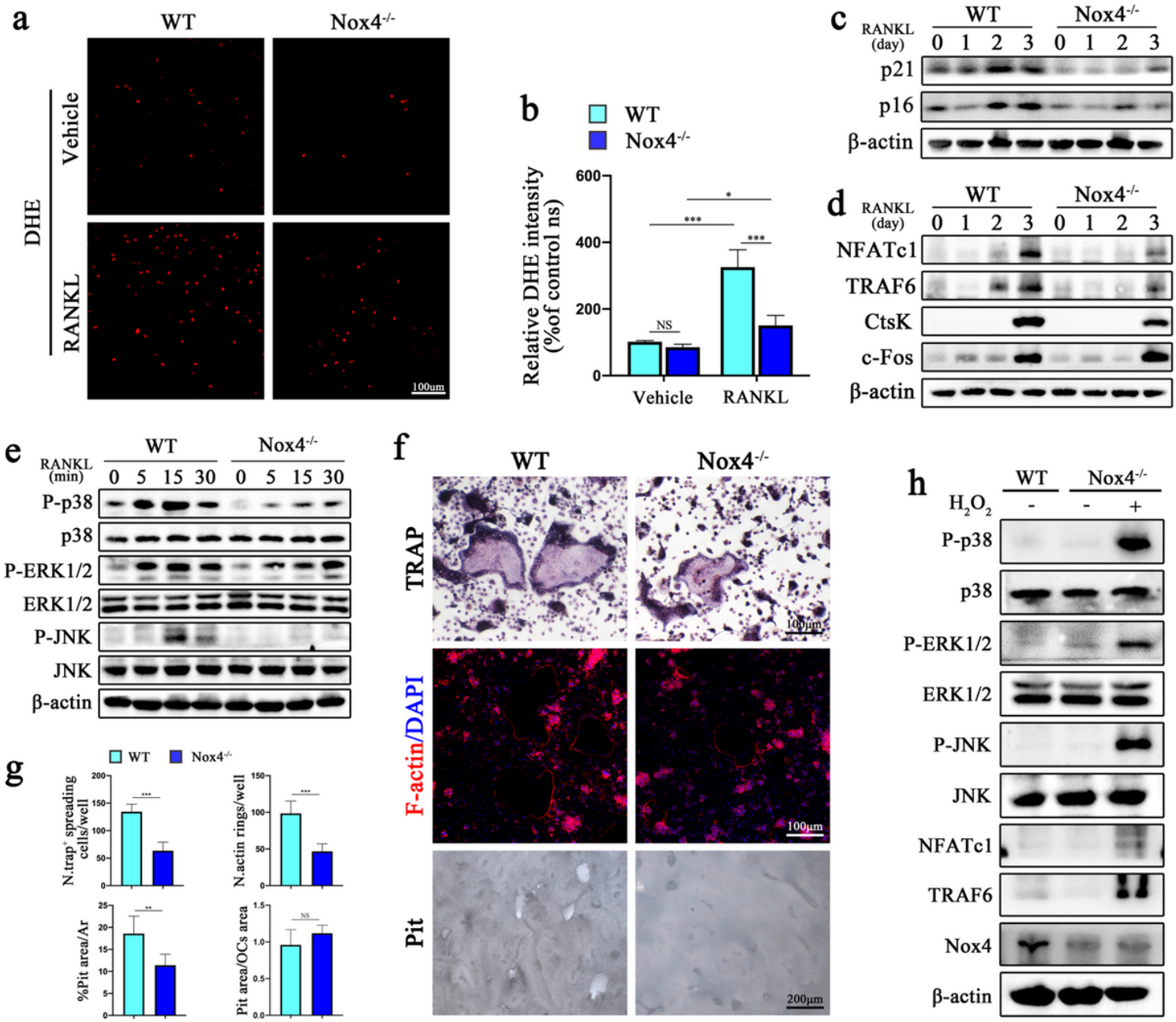

Figure 6

Osteoclast differentiation is dependent on Nox4-induced senescence. a Representative images of DHE fluorescence in WT and Nox4$^{-/-}$ OCPs stimulated with or without 100 ng/ml RANKL and 2mM NAC for 20 min. Scale bar: 100 μm. **b** Relative DHE intensities in OCPs under the indicated conditions. **c** Representative immunoblot images for senescence marker proteins in WT and Nox4$^{-/-}$ OCPs stimulated by 70ng/ml M-CSF and 100ng/ml RANKL for 0, 1, 2, 3 days. **d** Representative immunoblot images for osteoclast differentiation marker proteins in WT and Nox4$^{-/-}$ OCPs stimulated by 70ng/ml M-CSF and 100ng/ml RANKL for 0, 1, 2, 3 days. **e** Representative immunoblot images for MAPK signal pathway proteins in WT and Nox4$^{-/-}$ OCPs stimulated by 70ng/ml M-CSF and 100ng/ml RANKL for 0, 5, 15, 30 minutes. **f** Representative images for TRAP^{+} osteoclasts (**f** top, scale bar, 100 μm), actin belt (**f** middle,

scale bar, 100 μm) and bone resorption by osteoclasts (**f** bottom, scale bar, 200 μm). **g** Quantified analyses of $TRAP^+$ spreading multinucleated cells/well (**g** left top), actin belts/well (**g** right top), Pit area (**g** left bottom) and Pit area/OCs area (**g** right bottom). **h** Representative immunoblot images for osteoclast differentiation and MAPK signal pathway proteins stimulated by 70ng/ml M-CSF and 100ng/ml RANKL in WT OCPs and $Nox4^{-/-}$ OCPs with or without 0.5mM H_2O_2 for 24h. Data are shown as mean ± s.d. and analyzed by one-way ANOVA. n=5, ***P < 0.001 and ns ≥ 0.05.

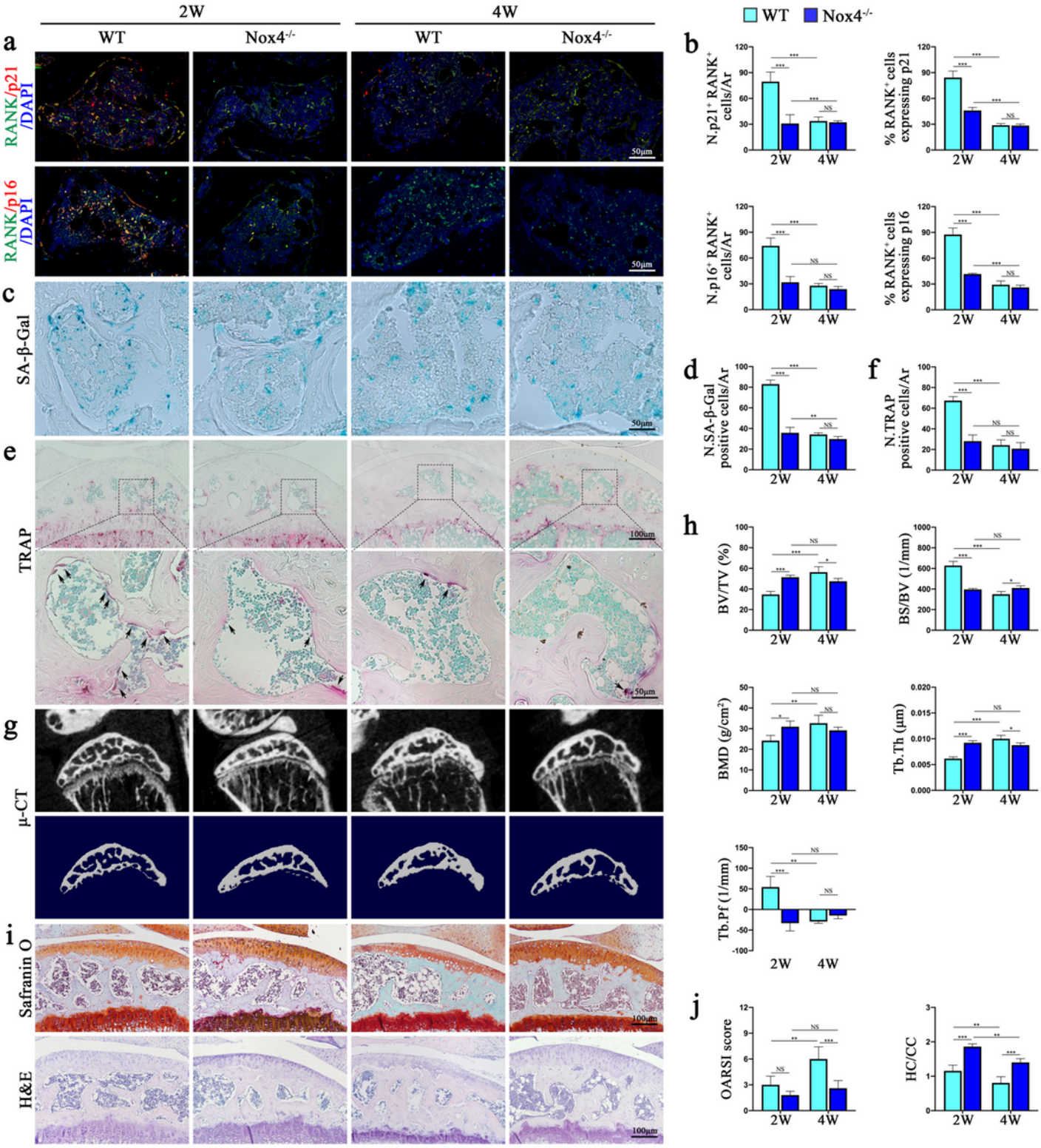

Figure 7

Knockout of Nox4 inhibits OCPs senescence and osteoclastogenesis to retar bone remodeling. a-j Three-month-old WT and Nox4$^{-/-}$ C57BL/6N mice were treated with ACLT and euthanized 2 or 4 weeks after surgery. **a** Representative images of double-immunofluorescence staining using antibodies against p21 (red, top), p16 (red, bottom) and RANK (green) of the tibial subchondral bone at 2 and 4 weeks post-ACLT in Nox4$^{-/-}$ mice compared with WT mice. Scale bar: 50 μm. **b** Quantified numbers of p21 and RANK

double-positive cells (top left), p16 and RANK double-positive cells (bottom left), and percentage of $RANK^+$ cells expressing p21 (top right) and p16 (bottom right) per mm^2 tissue area in mouse tibial subchondral bone at 2 and 4 weeks post-ACLT compared with that of the sham control. **c, d** SA-β-Gal staining and quantified numbers of SA-β-Gal^+ cells in mouse tibial subchondral bone at 2 and 4 weeks post-ACLT compared with that of the sham control. Scale bar: 50 μm. **e, f** Representative images and quantified numbers of $TRAP^+$ cells in subchondral bone. Scale bar: 100 μm (e top), 50 μm (e bottom). **g** Representative μ-CT images of sagittal views of the subchondral bone medial compartment in mice. **h** Quantitative analyses of trabecular bone volume fraction (BV/TV), bone surface area to bone volume ratio (BS/BV), bone mineral density (BMD), trabecular thickness (Tb.Th) and trabecular bone pattern factor (Tb.Sp). **i** Representative Safranin O-Fast green and H&E staining of sagittal sections of tibia articular cartilage and subchondral bone in ACLT OA mice. Scale bar: 100 μm. **j** Calculation of Osteoarthritis Research Society International (OARSI) scores (left) and quantitative analysis of tibial subchondral bone of HC/CC ratio in cartilage (right). Data are shown as mean ± s.d. and analyzed by two-way ANOVA. n=5, ***P < 0.001, **P < 0.01, *P < 0.05, and ns ≥ 0.05.

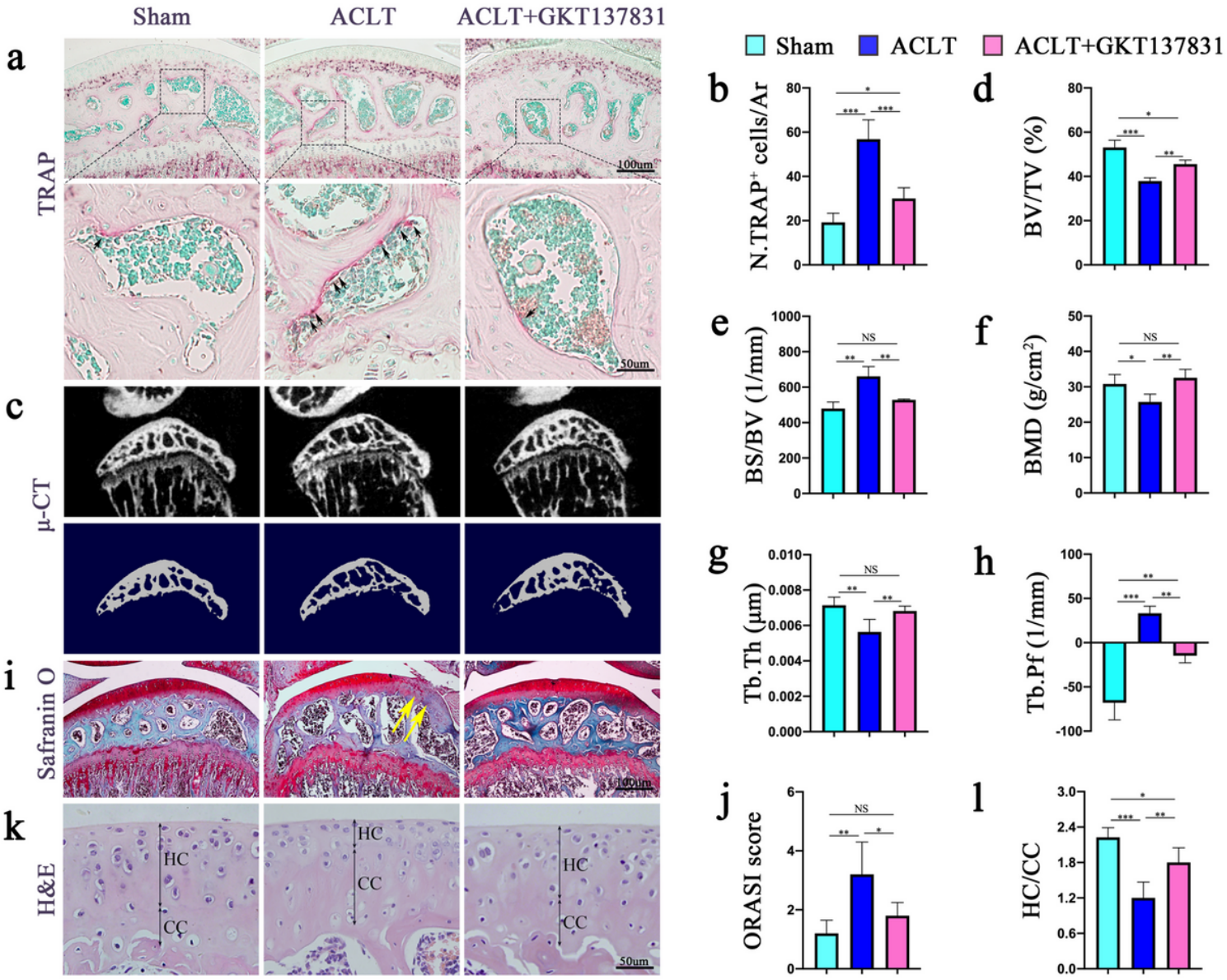

Figure 8

Administration of GKT137831 in vivo ameliorates OA progression. a-l Three-month-old C57BL/6N mice were treated with sham operation, ACLT, ACLT + 60mg/kg/d GKT137831. All the mice were euthanized 2 weeks after surgery. **a** Representative images for TRAP-stained tibia subchondral bone. Scale bar: 100 μm (top), 50 μm (bottom). **b** Numbers of $TRAP^+$ cells in subchondral bone per mm^2 tissue area. **c** Representative μCT sagittal views of the subchondral bone medial compartment in mice. **d-h** Quantitative analyses of trabecular bone volume fraction (BV/TV) (**d**), bone surface area to bone volume ratio (BS/BV) (**e**), bone mineral density (BMD) (**f**), trabecular thickness (Tb.Th) (**g**), and trabecular bone pattern factor (Tb.Sp) (**h**). **i** Safranin O–fast green staining of the tibia subchondral bone medial compartment (sagittal view). Scale bar: 100 μm. **j** Calculation of Osteoarthritis Research Society International (OARSI) scores. **k** Representative images for H&E staining where double-headed arrows marks the thickness of calcified cartilage (CC) and hyaline cartilage (HC). Scale bars: 50 μm. **l** Quantitative analysis of tibial subchondral

bone of HC/CC ratio in cartilage. Data are shown as mean ± s.d. and analyzed by one-way ANOVA. n=5, ***P < 0.001, **P < 0.01, *P < 0.05, and ns ≥ 0.05.

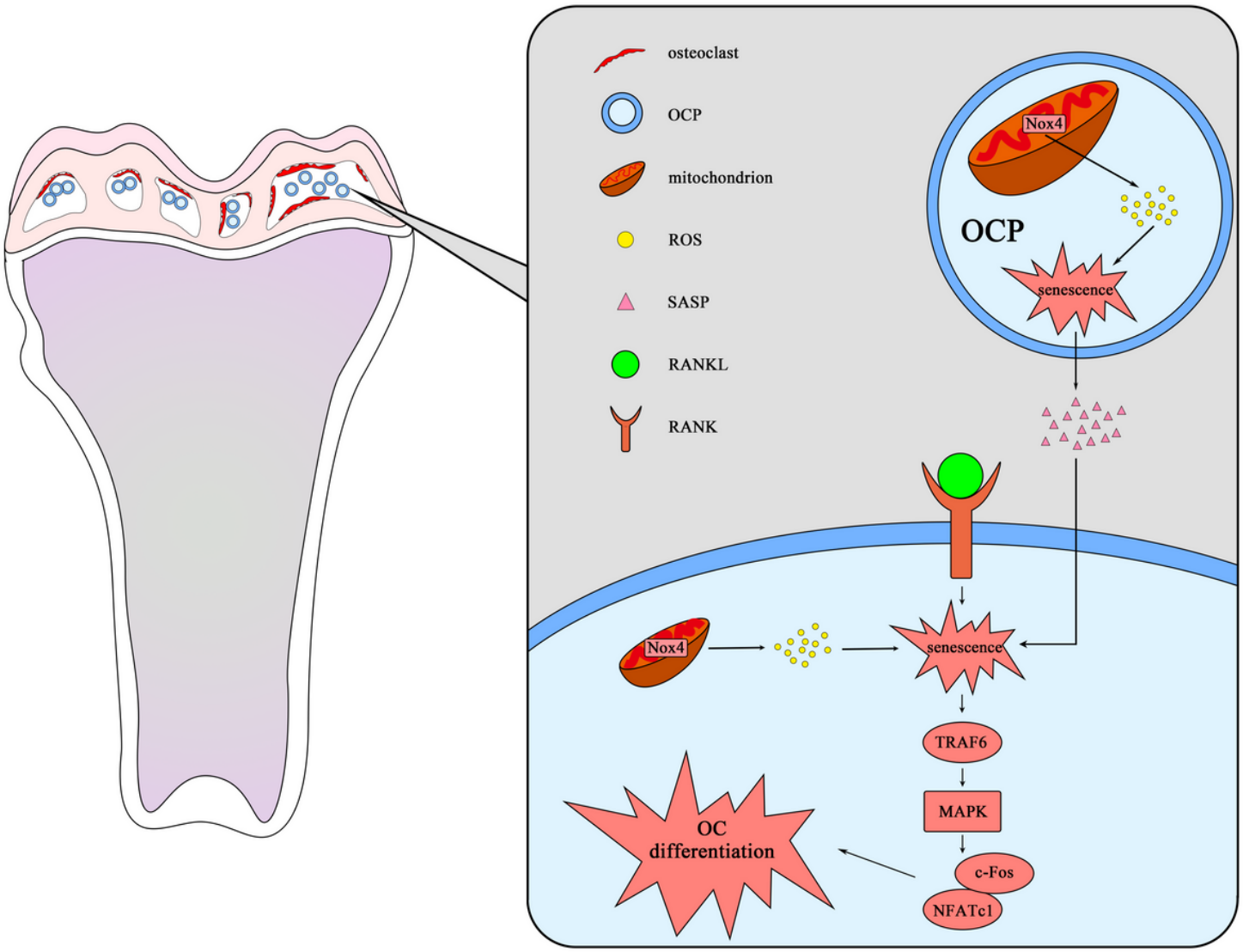

Figure 9

The mechanism of nox4-mediated senescence of OCPs promotes osteoclast differentiation in early OA. Nox4 expression is elevated in a subset of OCPs in early OA and induces OCPs senescence through the production of excess ROS. On one hand, the senescence of OCPs mediated by Nox4/ROS may be an essential step in initiating osteoclast differentiation. On the other hand, senescent OCPs secrete SASP factors to spread the senescence in OCPs clusters, over-activating the TRAF6/MAPK/c-Fos/NFATc1 axis in OCPs to accelerate the fusion of whole cellular clusters and osteoclast differentiation.